npj computational materials

www.nature.com/npjcompumats

ARTICLE OPEN

Check for updates

Photoinduced small electron polarons generation and recombination in hematite

Cheng Cheng[1], Yonghao Zhu[1], Zhaohui Zhou[2]✉, Run Long[1]✉ and Wei-Hai Fang[1]

Polarons generally affect adversely the photochemical and photophysical properties of transition metal oxides. However, the excited-state dynamics of polarons are not fully established to date and thus require an atomistic understanding. We focus on α-Fe_2O_3 with photoexcitation, electron injection, and heterovalent doping as the small polaron models, and conduct simulations of ab initio adiabatic molecular dynamics (AIMD) and nonadiabatic molecular dynamics (NA-MD). The elaborately designed AIMD simulations show that localization of electron at a single Fe site is an adiabatic and ultrafast process within sub-15 fs. Fe_2O_3 doping with an electron or a Si and Ti dopant forms a localized electron polaron while photoexcitation forms localized electron and hole polarons simultaneously, leading to diverse electron–hole recombination dynamics. NA-MD simulations demonstrate that recombination of an electron polaron created by doping with a delocalized hole at the valence band maximum of α-Fe_2O_3 takes place around 5 ps, while recombination between a pair of small electron and hole polarons in photoexcited Fe_2O_3 delays to about 110 ps owing to weak NA coupling and fast decoherence process. The ultrafast formation of small electron polarons in α-Fe_2O_3 impedes the accumulation of delocalized holes in the valence band that directly participate in water oxidation at photoanodes. The detrimental effect can be partially circumvented in photoexcited Fe_2O_3 for slowing electron–hole recombination despite polarons may retain low charge mobility. These findings provide a fundamental understanding of the excited-state dynamics of small electron polaron in α-Fe_2O_3 and may help design efficient transition metal oxides photoanodes.

npj Computational Materials (2022)8:148 ; https://doi.org/10.1038/s41524-022-00814-7

INTRODUCTION

Hematite (α-Fe_2O_3, hereafter Fe_2O_3), one of the most important transition metal oxides (TMOs), shows widespread applications, for example, corrosion, iron-cycling in geochemistry and biochemistry, dye-sensitized solar cells[1], and photoelectrochemical (PEC) cells[2]. During the last several decades, especially, PEC water splitting has turned out to be a potential technique in alleviating the global energy issues by generating clean hydrogen fuel[3–5]. Fe_2O_3 is considered to be a promising photoanode material for PEC water splitting[6], due to its advantages such as visible light response (bandgap of ~2.1 eV), valence band potential positive for water oxidation, long-term stability in neutral and alkaline solutions, low cost, earth-abundance, and nontoxicity[7]. However, the reported conversion efficiencies of solar energy into hydrogen are still left far behind its theoretical value of ~16.8%[8], due in part to the low solar-to-chemical conversion efficiencies of hematite photoanodes[6,8].

The low PEC efficiency for Fe_2O_3 was primarily assigned to its small charge carrier mobility, short charge carrier lifetime, and sluggish kinetics of oxygen evolution reaction[2,9]. Early studies of ex situ ultrafast transient absorption indicated that the charge recombination in Fe_2O_3 is ultrafast, nonradiative, and multi-exponential[10–16]. Later on, the dynamics of hole charge gained ever-growing attention due to the water oxidation at Fe_2O_3 photoanodes deployed in PEC cells. The lifetime of photogenerated holes in Fe_2O_3 was reported to be about three orders of magnitude shorter than that in TiO_2[17], which however can be extended to microseconds with electric bias by suppressing electron–hole recombination[18–22].

Recently, the Fe_2O_3 polarons dynamics got special interest due to the rapid development of new experimental techniques. Polarons are formed by self-trapping charge carriers and simultaneously deforming the local lattice, thus generally causing small charge-transport ability and manifesting strong electron–phonon interaction. The concept of polarons[23] was initially introduced in Fe_2O_3 to rationalize the abnormally low charge mobility[24,25], which is about 10^5 times smaller than that of the conventional silicon semiconductor[6,26]. Experimental confirmation of electron polarons (EPs) in Fe_2O_3 was for the first time reported by Katz et al. by using time-resolved X-ray transient absorption spectroscopy (TAS) over Fe_2O_3 nanoparticles with excess electrons injected from photoexcited dye molecules[27,28]. After that, some groundbreaking experiments opened new avenues for exploring the roles of polarons in the excited-state dynamics of Fe_2O_3[29–32], which turn out to be key issues affecting the performance of Fe_2O_3 photoanodes, for example, ultrafast trapping of photoexcited charge carriers[7,30–34] and poor device photovoltage[6].

By using femtosecond extreme ultraviolet TAS, Carneiro et al. reported that the formation of polarons in Fe_2O_3 began within 100 fs, the formation process continued for about 2–3 ps, and the decay process lasted for more than 300 ps under several optical excitations[30]. Biswas et al. observed a similar process for the formation of electron and hole polarons in Fe_2O_3 by using femtosecond extreme ultraviolet reflection–absorption spectroscopy[32]. However, a timescale of 660 fs was attributed to surface trapping of the photoexcited EP formation which is demonstrated to be irrelevant to grain boundaries and surface defects and thus intrinsic to Fe_2O_3[31,32]. Recently, an in situ observation of EPs re-excitation in Fe_2O_3 PEC cells was reported by Pastor et al.[34] through using the pump–push photocurrent detection and TAS, which offers a strong argument for the formation of EP in

[1]College of Chemistry, Key Laboratory of Theoretical & Computational Photochemistry of Ministry of Education, Beijing Normal University, 100875 Beijing, China. [2]Chemical Engineering and Technology, School of Water and Environment, Chang'an University, 710064 Xi'an, China. ✉email: zzhlax@chd.edu.cn; runlong@bnu.edu.cn

Fe_2O_3 and its role in the PEC performance. A timescale of 600 fs was reported therein and attributed to the localization of delocalized electrons to the polaronic state.

On the other side, substantial efforts have been devoted to theoretical simulations on the properties of EPs and hole polarons (HPs) in Fe_2O_3[35–38]. It has been demonstrated that the related properties depend on the choices of cluster or extended systems and Hartree–Fock or density functional theory (DFT)-based electronic structure methods. For example, localization of HPs on Fe or O sites or both is still in debate in both experiment[39–42] and simulation[37,38]. In the framework of Marcus's theory, transport of EPs and HPs in Fe_2O_3 and the effect of dopants were investigated by using both cluster and extended models with unrestricted Hartree–Fock, complete active space self-consistent field[43–46], or DFT at the level of generalized gradient approximation (GGA), including Hubbard correction (U)[26,47]. Our previous work based on ab initio molecular dynamics (AIMD) simulations visualized the hopping process of an EP in Fe_2O_3 and uncovered the role of Si dopant in speeding up the polaron hopping[48]. To date, simulations on the excited-state dynamics of polarons in Fe_2O_3 are still unavailable, leading to a lack of insights which are fundamental for understanding the nature of excited states dynamics and thus the limitation factors related to the poor PEC performance of Fe_2O_3 photoanodes.

In this work, we aim to establish the mechanism for the dynamic processes of EP formation and EP interactions with free holes or HPs in Fe_2O_3 leading to nonradiative charge losses, which are rarely simulated because such simulations require advanced simulation methodologies[49]. In order to address these issues, we designed a scheme to access the timescale for the formation of small EPs in Fe_2O_3. This scheme is made up of a series of ab initio AIMD simulations with the initial structure for each simulation randomly sampled from the AIMD trajectory of pure Fe_2O_3 and meanwhile addition of an extra electron as a perturbation in charge density. The simulations show that EP formation is adiabatic with ultrafast electron motion at the timescale less than 15 fs, reasonably agreeing with the recent experiments[30–32,34]. Nonadiabatic molecular dynamics (NA-MD)[50,51] simulations combined with time-dependent density functional theory (TDDFT)[52–54] in the Kohn–Sham formulation were performed to study nonradiative recombination of EPs with photogenerated holes. Two types of recombination were considered, i.e., recombination of an EP with a delocalized hole in Fe_2O_3 with an electron, Si, or Ti atom doping and recombination of an EP with a localized hole in Fe_2O_3 with constrained electron and hole excitation. Our results show that EP recombination with delocalized hole takes place on about 5 ps, which is faster by a factor of about 20 than EP recombination with localized hole that proceeds more than 110 ps, which is in good agreement with the recent experiment[30]. The occurrence of long-lived EPs is attributed to the weak NA coupling and fast loss of coherence. This study offers us new insights of excited-state dynamics of polarons in Fe_2O_3 which are distinct from those in rutile TiO_2[49], and provide a concept for designing high-performance TMOs photoanodes from the viewpoint of polaron dynamics.

RESULTS AND DISCUSSION

To explore the excited-state dynamics of EPs in Fe_2O_3, two types of EP models were considered. Model I contains only an EP, which was obtained via either electron injection (e@EP) or foreign Si and Ti atom doping (Si@EP, Ti@EP), as shown in Fig. 1a, b. Si and Ti dopants were considered here because of the capability of donating an electron and the popularity in improving water oxidation at Fe_2O_3 photoanodes[2,55]. Model II contains simultaneously an EP and a localized hole, i.e., a small HP. Upon photoexcitation, the photoexcited electron and hole in Fe_2O_3 experience the delocalized states first, as shown in Fig. 1c and detonated as photon@DS, and then rapidly relax to the more stable localized states and form the EP and HP (photon@EP&HP), as shown in Fig. 1d.

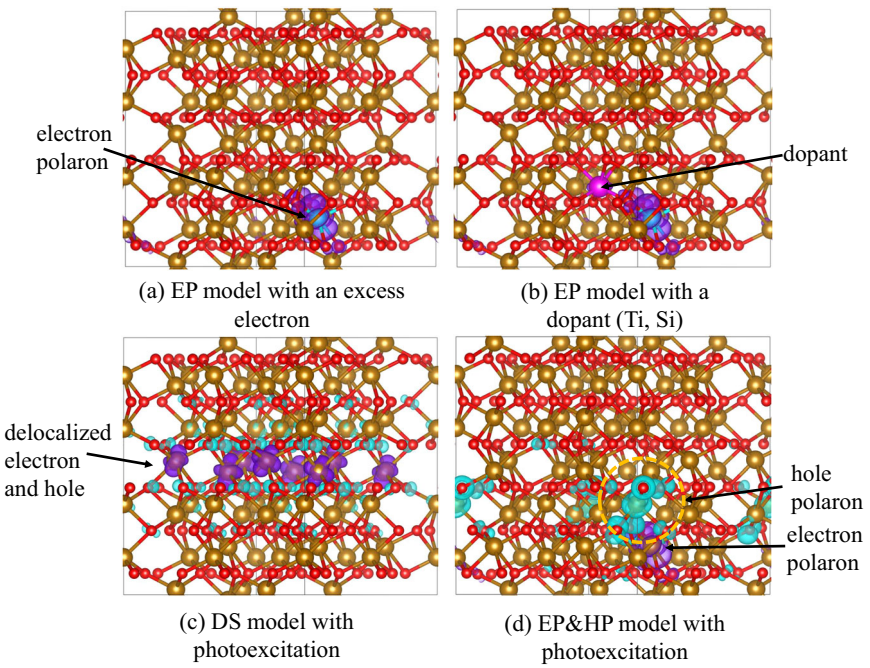

Fig. 1 Structures of two types of polarons in Fe_2O_3. EP localized at an Fe site in Fe_2O_3 with (**a**) injection of an excess electron, defined as e@EP, and (**b**) Si or Ti doping, defined as Si@EP or Ti@EP. Photoexcited electron and hole in Fe_2O_3 of (**c**) delocalized states, defined as photon@DS, and (**d**) localized states, defined as photon@EP&HP for which a dashed orange circle highlights the HP localized at a Fe atom (green) and its six coordinating O atoms (blue). Fe^{3+}, Fe^{2+}, O^{2-}, and dopant atoms were depicted in brown, cyan, red, and carmine, respectively, and the isosurfaces of electron and hole charge densities are shown in purple and cyan.

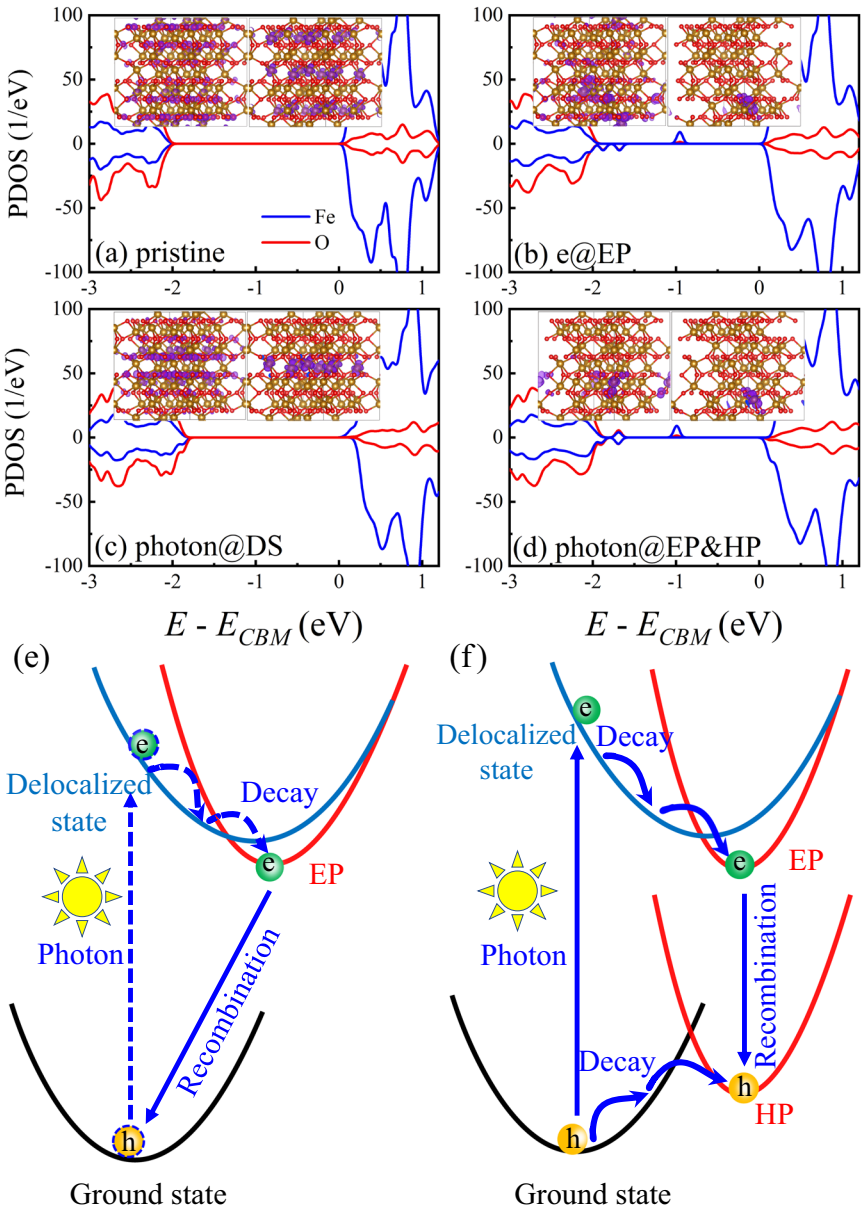

Fig. 2 Electronic structures for two type of polarons in Fe_2O_3 and the corresponding charge recombination processes. Projected DOS for (**a**) pure Fe_2O_3, **b** e@EP, **c** photon@DS, and (**d**) photon@EP&HP. The insects indicate the charge densities of the VBM and CBM state in (**a**), the VBM and EP state in (**b**), the VBM and CBM state in (**c**), and the EP and HP state in (**d**). Analyses are focusing on the spin-up component in which polarons are present in the defective systems. Schematic potential energy surfaces for describing two type of charge recombination processes of (**e**) the EP and the delocalized hole at VBM in e@EP and (**f**) the EP and HP in photon@EP&HP. Note that the photoexcitation and subsequent electron trapping by EP in (**e**) are hypothetical processes which are represented by the dashed line (photoexcitation) and circles (electron and hole), but they are simulated processes in (**f**) by using ΔSCF and are represented by the solid line and circles.

Geometric and electronic structure of EPs at 0 K

The formation of small polarons in Fe_2O_3 is sensitive to the Fe–O bond length[48,56]. The calculated average Fe^{3+}–O bond length is 2.04 Å in the pure Fe_2O_3, which was elongated to 2.11, 2.13, and 2.11 Å for the average Fe^{2+}–O bond length during polaron formation in e@EP, Si@EP, and Ti@EP, respectively, associated with the reduction of an Fe^{3+} ion to an Fe^{2+} ion and lattice expansion. The Fe^{2+}-O bond elongation by ~0.08 Å is consistent with the previous investigations[35,36]. For photon@EP&HP, photoexcitation induces the redox reaction in Fe_2O_3, giving rise to the average Fe^{2+}-O bond length of 2.12 Å and Fe^{4+}–O bond length of 1.99 Å due to the larger radius of Fe^{2+} than Fe^{3+} and the smaller radii of Fe^{4+} and O^- than Fe^{3+} and O^{2-}. The computed magnetic moment on an Fe^{3+} ion in the pure Fe_2O_3 is 4.14 μ_B. After electron injection and Si or Ti doping, an Fe^{3+} ion is reduced to an Fe^{2+} ion with the local magnetic moments decreased to 3.62 μ_B in e@EP, 3.67 μ_B in Si@EP and 3.64 μ_B in Ti@EP. For photon@EP&HP, the magnetic moment of an Fe^{3+} ion is reduced to 3.63 μ_B of an Fe^{2+} ion which is assigned to the EP and to 3.70 μ_B of an Fe^{4+} ion which is attributed to the HP, while the changes in the magnetic moments of the six O atoms coordinating the Fe^{4+} ion are relatively small. The calculated magnetic moments of the Fe^{2+} ions agree well with the previous report[48], and the change in the magnetic moment of Fe^{4+} relative to Fe^{3+} is similar to that obtained using the PBE0 functional with low fraction of the exact exchange[37]. To determine the location of the EP site, we calculated the total energies of all possible EP sites in the Si- and Ti-doped Fe_2O_3 supercell and compared their energy

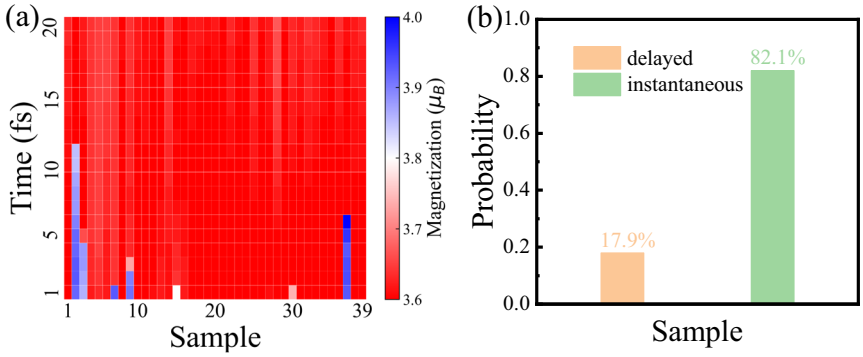

Fig. 3 Ultrafast electron polaron formation in Fe_2O_3. a Evolution of the interested Fe magnetic moment in the first 20 fs of the AIMD simulation on each structure which was prepared by adding an electron in the snapshot sampled from the trajectory of pure Fe_2O_3. More details can be found in Supplementary Fig. 4. **b** Probability of the two types of EP formation derived from the 39 AIMD simulations. "instantaneous" means an EP was formed at the first step of the AIMD simulation and "delayed" means after a period of time an EP was formed.

difference with respect to the most stable EP, as shown in Supplementary Fig. 1. The same Fe ion was chosen for the e@EP.

Figure 2 shows the projected density of states (PDOS) and charge densities of the valence band maximum (VBM), conduction band minimum (CBM) and polaron states of pure Fe_2O_3, e@EP, photon@DS and photon@EP&HP. For pure Fe_2O_3, the VBM and CBM are composed primarily of O 2p and Fe 3d orbitals, respectively, see Fig. 2a. For e@EP, the EP occurs as a mid-gap state with the electron charge localized at an Fe site and the VBM remains delocalized over majority of the supercell, see Fig. 2b. Similarly, Si and Ti doping also lead to localized EPs and delocalized VBMs[36,48,57], as shown in Supplementary Fig. 2. Following photoexcitation of pure Fe_2O_3, electrons in the VB would be promoted into the CB. Figure 2c shows a pair of delocalized CBM electron and VBM hole. Driven by electron-vibrational interaction, the delocalized electron and hole further decay and form a pair of stable EP and HP accompanied with local lattice distortion. As shown in Fig. 2d, the EP is localized at an Fe site and the HP is resided around another Fe site and the six O atoms next to it, which is similar to the recent theoretical simulation of Fe_2O_3 by using the HSE functional with 12% of exact Exchange[38]. The enlarged PDOS shown in Supplementary Fig. 3 shows that the EP and HP states are dominated by the Fe-*d* orbital and the hybridized Fe-*d* and O-*p* orbitals, respectively, agreeing well with the charge density analysis.

AIMD simulations of EP formation dynamics

The experiment confirmed that EPs can be formed in Fe_2O_3 by electron injection from photoexcited dye molecules[58]. However, how the EP was formed in Fe_2O_3 at atomistic level remains unclear yet. According to our previous work[48], the transition of the local magnetic moment on an Fe ion from ~4.1 to 3.6 μ_B corresponds to the electron transfer from Fe^{3+} to Fe^{2+}, thus demonstrating the EP formation. Figure 3a shows two types of EP formation in the current AIMD simulations, i.e., instantaneous EP formation in most cases and delayed EP formation in few cases. The possibility of the two types of EP formation is summarized in Fig. 3b. The former arises due to the initial structures with appropriate Fe–O bond lengths to accommodate EPs. However, the latter conveys an important message that the EP formation proceeds with the added electron changing from a delocalized meta-stable state to a localized stable state. This process is adiabatic with the timescale of sub-15 fs, which is ultrafast in relation to the EP recombination (see below). We notice that the formation time is shorter than the values from two experimental reports[30,34]. The discrepancy can be attributed to the hot electron relaxation within the CB which was not considered here. The hot electron relaxation is a common process in experiments where electrons in the VB were pumped with 400 nm light to the CB[34]. According to our previous report, the process took about 100 fs to the CBM although the specific values depended on the initial state above CBM[59]. Taking this situation in mind, the current simulations agree well with the experiments[30,34]. For more details of the EP formation in Fe_2O_3, refer to Supplementary Fig. 4. The calculated energy to re-excite the EP to the delocalized state within CB is about 1.08 eV and agrees well with a previous report[34], which is much larger than the thermal energy at room temperature ($k_BT = 0.025$ eV). The ultrafast EP formation by self-trapping of free electrons reduces charge carrier mobility and is expected to be detrimental to PEC water oxidation. As reported recently, re-excitation of EPs in Fe_2O_3 by near-IR light correlates well with the improvement in photocurrent of Fe_2O_3 photoanodes[34]. Consequently, retarding the self-trapping process or re-exciting EPs to the CB may be alternative strategies to alleviate the ultrafast EP formation and improve the water oxidation at Fe_2O_3 photoanodes.

NA-MD simulations of EP recombination dynamics

In the current NA-MD simulations, the initial state for the first type of EP recombination is the excited state composed of an EP and a VBM hole, see Fig. 2e. This initial state was prepared by assuming photoexcitation of an electron from the VBM to the CBM with a hole remained at the VBM in Fe_2O_3 containing an EP, corresponding to the e@EP, Si@EP, and Ti@EP systems. The charge distribution of the EP and VBM in each ground state was shown in the inset of Fig. 2b for e@EP and Supplementary Fig. 2 for Si@EP and Ti@EP. In the second type of EP recombination, the initial state corresponds to the excited state composed of an EP and an HP (photon@EP&HP), see Fig. 2f. In this case, the initial state was prepared using ΔSCF by photoexcitation of an electron from the VBM to the CBM of pristine Fe_2O_3 ground state followed by interacting with lattice, leading to formation of an EP and an HP. The charge distribution of the EP and HP of this excited state is shown in the inset of Fig. 2d.

Electron-vibrational interaction. Nonradiative charge recombination correlates with electron-vibrational interactions. Figure 4a, b shows time evolution of the energies of all the states involved in the EP recombination processes. The energies of the EP and HP states for photon@EP&HP fluctuate more violently than those of the EP and VBM states for e@EP, suggesting stronger electron-vibrational interactions in the former system. The coherence between the pairwise states was further inspected by unnormalized autocorrection functions (un-ACF) of the phonon-induced fluctuation in the energy gaps, i.e., EP-HP for the photon@EP&HP and EP-VBM for the e@EP, as shown in Fig. 4c. Generally, larger

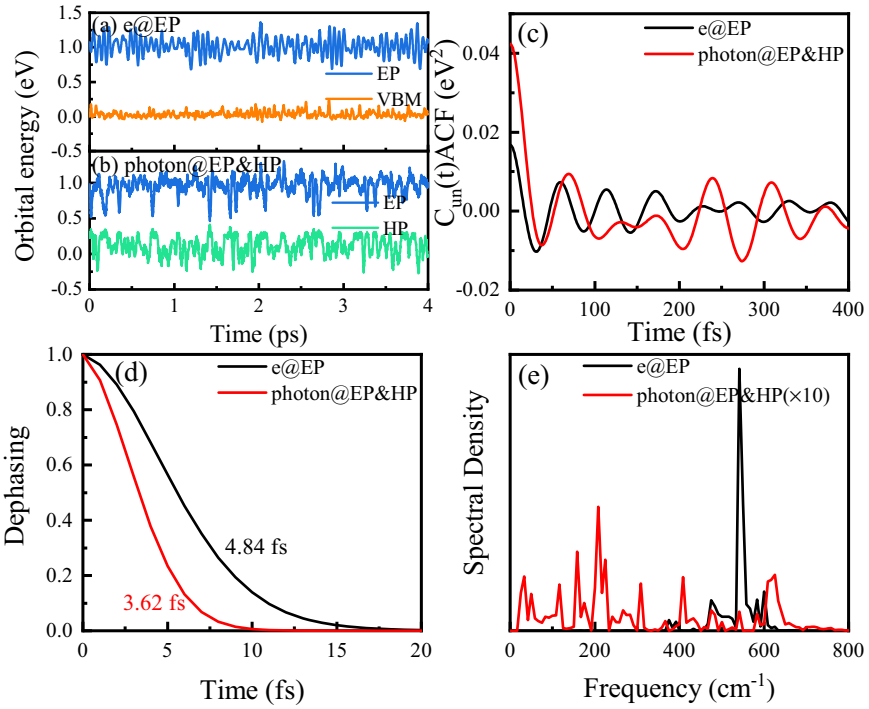

Fig. 4 Electron-vibrational interaction for e@EP and photon@EP&HP. Evolution of the orbital energies of (**a**) the localized EP and delocalized VBM states for e@EP and (**b**) the localized EP and HP states for photon@EP&HP, (**c**) unnormalized autocorrelation functions derived from the two energy gaps, (**d**) pure-dephasing functions, and (**e**) influence spectra of EP-VBM for e@EP and EP-HP for photon@EP&HP.

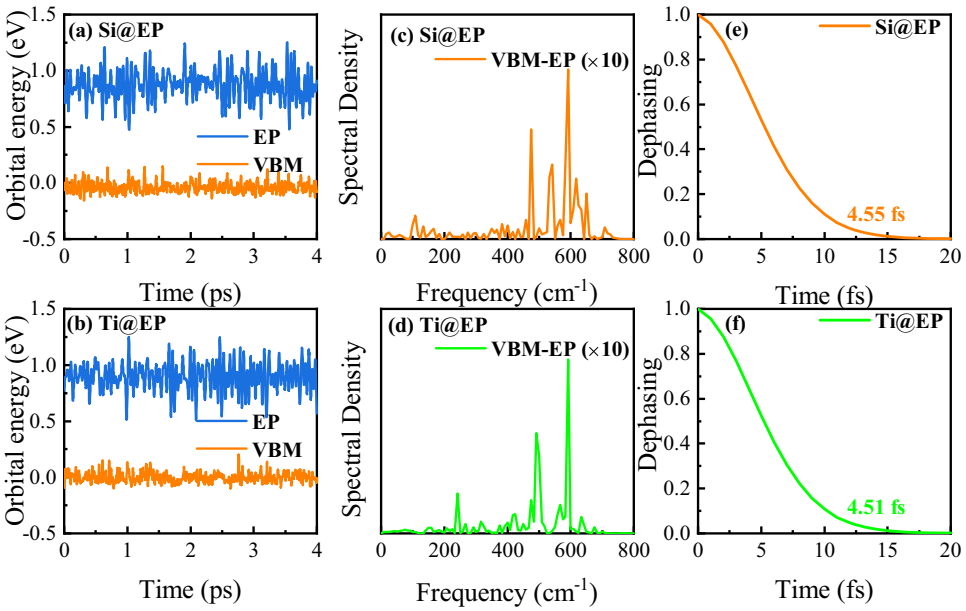

Fig. 5 Electron-vibrational interaction for Si@EP and Ti@EP. a, **b** Evolution of the orbital energies of the EP and VBM states, (**c**, **d**) influence spectra, (**e**, **f**) pure-dephasing functions for Si@EP and Ti@EP.

initial value, slower and more asymmetric decay of un-ACF favor faster dephasing[60,61], especially the initial value[62]. The elastic charge−phonon scattering is responsible for the phonon-induced loss of coherence within the electronic subsystem, which is determined by the pure-dephasing function of the optical response theory[63]. Fits of the pure-dephasing functions derived by integrating the un-ACFs with the Gaussian function of exp $(-0.5(t/\tau)^2)$ lead to the pure-dephasing times τ of 3.62 and 4.84 fs for the photon@EP&HP and e@EP, respectively, as shown in Fig. 4d. Inelastic charge phonon scattering creates NA coupling and accommodates the excess energy lost during EP recombination. To identify the phonon modes that couple to the electronic transition, Fourier transforms of the un-ACF of the phono-induced fluctuations in the energy gap of EP-VBM of e@EP and EP-HP of photon@EP@HP were computed. Figure 4e exhibits multiple low-frequency phonon modes in the photon@EP&HP, which correspond to the infrared- and Raman-active vibrational modes observed experimentally[64]. The sum of them surmounts the

high-intensity major peak around 550 cm^{-1} in the e@EP that is similar to the vibrational mode occurring in Fe_2O_3 with an oxygen vacancy[59], driving faster pure-dephasing.

Figure 5a, b shows that time evolution of the energies of the EP and VBM states for the Si@EP and Ti@EP. The energy of the EP states fluctuates slightly more violently than that of e@EP, see Fig. 4a. Fourier transforms of the un-ACF of the fluctuation in the EP-VBM energy gap characterize the vibrational modes participating in the EP recombination, see Fig. 5c, d. The infrared- and Raman-active vibrational modes observed experimentally[64] appeared for Si@EP and Ti@EP as well, which are similar to those in photon@EP&HP but activate more phonon modes with low intensities due to symmetry breaking induced by dopants. The high-frequency modes around 600 cm^{-1} dominate the influence spectra and lead to strong NA coupling. The presence of multiple phonon modes leads to fast loss of coherence, corresponding to the pure-dephasing times of 4.55 and 4.51 fs for Si@EP and Ti@EP, respectively, see Fig. 5e, f, which are very close to 4.84 fs for e@EP. The similar pure-dephasing times of the Si@EP and Ti@EP systems are attributed to the similar spectral densities, see Fig. 4e.

Nonradiative charge carrier recombination

Population evolution of EP states in the four models is shown in Fig. 6, and fitting the decay curves to the exponential function, $P(t) = \exp(-t/\tau)$, gives the recombination time τ. The recombination between the EP and HP state is estimated to proceed about 110 ps, in good agreement with the lifetimes reported in recent experiments[16,30]. The recombination time is about 26 times larger than the time of 4.2 ps between the EP and VBM state for e@EP, greatly prolonging the lifetime of EPs. The recombination times of 5.1 and 5.6 ps for Si@EP and Ti@EP are slightly longer than that for e@EP, consistent with the experimental observation in ref. [14] that

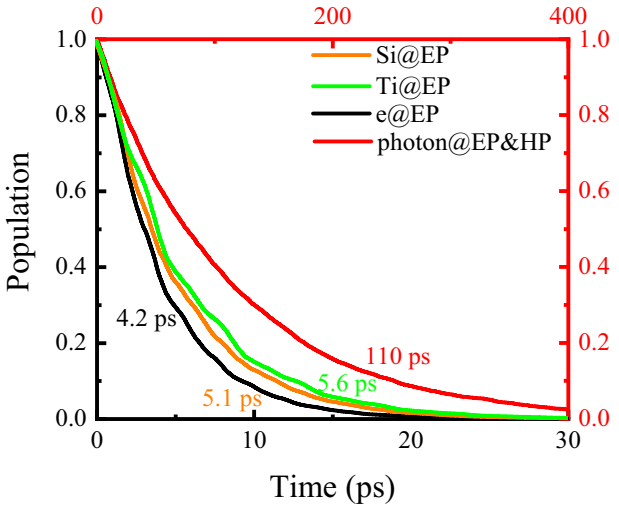

Fig. 6 Population of polaron states for e@EP, Si@EP, Ti@EP, and photon@EP&HP. Note the different scales of the time axes for e@EP, Si@EP and Ti@EP, and photon@EP&HP.

the charge carrier dynamics in Ti-doped Fe_2O_3 are slightly slower than in the unintentionally doped sample. The charge recombination rate depends on the NA coupling, energy gap and dephasing time which are summarized in Table 1 for the four systems. The average NA coupling between the EP and HP state is 1.61 meV, which is significantly smaller than 8.40, 7.50, and 6.90 meV between the relavent pairwise electronic states for e@EP, Si@EP, and Ti@EP, respectively. Besides, the larger fluctuation in the energy gap between the localized EP and HP state gives rise to a shorter decoherence time than in the other three systems. The weaker NA coupling and faster decoherence effect contribute mainly the slower EP recombination dynamics with the HP despite the energy gap is slightly smaller.

The simulations greatly extend understanding of the EP generation and recombination dynamics in Fe_2O_3 toward the PEC water oxidation. The localized EPs recombine fast with the delocalized VBM holes, accumulation of which is expected to be substantial for water oxidation at photoanodes. In contrast, photoexcitation upon Fe_2O_3 generates simultaneously localized EPs and HPs which create weak NA coupling and fast decoherence between the two states, leading to slow charge recombination and prolonged EP lifetime. These findings disobey the intuition that small polarons facilitate the electron–hole recombination and offer a piece of evidence which directly support the conclusions of the extreme ultraviolet spectroscopy experiments which indicated prolonged polarons lifetimes upon photoexcitation of Fe_2O_3[31]. Generally, small polaronic states should be avoided in transition metal oxides for solar energy conversion, and some methods may be worth having a try, such as excitation energy increasement[30], co-doping[65], and formation of multinary oxides[34]. Very recently, the concept of self-trapped exciton was proposed to rationalize the Auger recombination in Fe_2O_3[66–68], which is however beyond the scope of this work.

To summarize, the excited-state dynamics of EPs in Fe_2O_3 have been systematically investigated by using both AIMD and NA-MD simulations. The elaborately designed AIMD simulations establish the adiabatic mechanism of the EP formation which is ultrafast with a timescale of sub-15 fs. Taking into account the process of hot electron relaxation in the CB, the EP formation time agrees well with the experiment. Electron injection, Si, or Ti doping generate localized EPs in Fe_2O_3, while photoexcitation generates pairwise localized EPs and HPs. The different nature of the polarons affect notably the electronic structure and recombination dynamics. The NA-MD simulations show that recombination of an EP with a delocalized VBM hole gives rise to the short EP lifetime while recombination between pairwise localized EP and HP extends significantly the EP lifetime. The reason is ascribed to the weaker NA coupling and faster loss of coherence in the latter case. The current work establishes the mechanisms of excited-state dynamics of EPs in Fe_2O_3, advances our understanding of the EP formation and recombination dynamics, and provides the knowledge of rational design of high-efficiency TMOs photoanodes.

Table 1. Canonically averaged energy gap, pure-dephasing time, average absolute NA coupling, and electron–hole recombination time for the electron–hole recombination in Fe_2O_3.

Systems	Energy gap (eV)	Dephasing (fs)	NA coupling (meV)	Recombination (ps)
Photon@EP&HP	0.85	3.62	1.61	110
e@EP	0.98	4.84	8.40	4.20
Si@EP	0.91	4.55	7.50	5.10
Ti@EP	0.90	4.51	6.90	5.60

METHODS

AIMD simulations of EP formation dynamics

To access the timescale of an EP formation in Fe_2O_3, a method combining AIMD simulations with a perturbation in charge density were proposed. The procedure was described as follows. First, a nuclear trajectory for pure Fe_2O_3 in equilibrium at room temperature was generated by running an AIMD simulation. Then, a number of structures were sampled randomly from the trajectory, including the atomic coordinates and velocities. Finally, a series of AIMD simulations were carried out with those initial structures each of which an electron was added into. The sudden injection of a foreign electron into the Fe_2O_3 lattice was thus deemed as a perturbation in the charge density of pure Fe_2O_3.

NA-MD simulations of EP recombination dynamics

NA-MD simulations of EP recombination process were carried out by the mixed quantum-classical dynamics methodology implemented within the time-dependent DFT in the Kohn–Sham (KS) representation[52]. ΔSCF was used to promote one electron from the VBM to the CBM to prepare the initial EP-HP state of photoexcited Fe_2O_3 which offers a simple method to describe the excited state in the condensed phases. The details about TDDFT procedure were shown in Supplementary Methods. The mixed quantum-classical approach treated lighter and faster electrons quantum mechanically, while described the heavier and slower nuclei classically. The classic path approximation (CPA)[69] is used to accelerate the calculation because CPA has been justified in condensed matter systems, in which the nuclear dynamics were steered by thermal fluctuations, and a single-electron excitation had little effect on the geometric structures and electronic dynamics. In order to test the validity of the CPA, we compared the changes in the geometries of Fe_2O_3 (Fig. 1d) induced by a delocalized electron and hole (Fig. 1c) with thermally induced atomic fluctuations in the ground state, and observed that the average Fe–O bond length is 1.967 in the excited state vs 1.966 Å in the ground-state geometries with negligible change of 0.001 Å, while the thermal fluctuations increased the Fe–O bond length to 1.972 Å. The thermal fluctuations show the bond length change a factor of 6 greater than the optimized geometry changes upon photoexcitation, indicating that the CPA was reasonable for the systems under investigation. Decoherence-induced surface hopping (DISH) algorithm[70] was introduced to rescale the nuclear velocity in the direction of the gradient NA coupling vector, $\langle \phi_i | \nabla_R | \phi_j \rangle$, after a quantum hop. When the decoherence time was significantly shorter than the quantum transition time, it strongly affects the transitions especially for carrier recombination across large bandgap. The approach has been applied to study excited state dynamics in metal oxides[59,71,72].

Simulation details

Geometry optimization and electronic structure calculations were carried out by using the VASP code within the framework of spin-polarized density functional theory[73]. To access the EP formation time in Fe_2O_3, an AIMD trajectory of 10 ps was generated first. Then, an electron was added in 39 snapshots chosen randomly from the thermally equilibrated portion of the trajectory to perform a new AIMD simulations with each lasting for 200 fs. Geometry optimization for the four EP structures were done first at 0 K and then heated to 300 K with repeated velocity rescaling for 2 ps. Four AIMD trajectories with each lasting 4 ps were generated in the microcanonical ensemble with the time step of 1 fs. Based on these trajectories, the NA-MD simulations were performed by using the Python eXtension for Ab initio Dynamics code[50,51] with 5000 stochastic realizations of the surface hopping algorithm which guarantees good statistical convergence. For more details on the NA-MD method, one can refer to the original works[50,51,74]. More details of the simulation are shown in Supplementary Simulation Details.

DATA AVAILABILITY

The data of this study are available from the lead corresponding author upon reasonable request via email: runlong@bnu.edu.cn.

Received: 2 November 2021; Accepted: 29 May 2022;
Published online: 07 July 2022

REFERENCES

1. Hou, Y. et al. Rational screening low-cost counter electrodes for dye-sensitized solar cells. *Nat. Commun.* **4**, 1583 (2013).
2. Sivula, K., Le Formal, F. & Grätzel, M. Solar water splitting: progress using hematite (α-Fe_2O_3) photoelectrodes. *ChemSusChem* **4**, 432–449 (2011).
3. Chen, X. et al. Semiconductor-based photocatalytic hydrogen generation. *Chem. Rev.* **110**, 6503–6570 (2010).
4. Chen, S., Takata, T. & Domen, K. Particulate photocatalysts for overall water splitting. *Nat. Rev. Mater.* **2**, 17050 (2017).
5. Lumley, M. A. et al. Perspectives on the development of oxide-based photocathodes for solar fuel production. *J. Am. Chem. Soc.* **141**, 18358–18369 (2019).
6. Lohaus, C., Klein, A. & Jaegermann, W. Limitation of fermi level shifts by polaron defect states in hematite photoelectrodes. *Nat. Commun.* **9**, 4309 (2018).
7. Kay, A. et al. Effect of doping and excitation wavelength on charge carrier dynamics in hematite by time-resolved microwave and terahertz photoconductivity. *Adv. Funct. Mater.* **30**, 1901590 (2019).
8. Shen, S. et al. Hematite heterostructures for photoelectrochemical water splitting: rational materials design and charge carrier dynamics. *Energy Environ. Sci.* **9**, 2744–2775 (2016).
9. Bandaranayake, S. et al. Small polarons and surface defects in metal oxide photocatalysts studied using xuv reflection–absorption spectroscopy. *J. Phys. Chem. C.* **124**, 22853–22870 (2020).
10. Cherepy, N. J. et al. Ultrafast studies of photoexcited electron dynamics in γ- and α-Fe_2O_3 semiconductor nanoparticles. *J. Phys. Chem. B* **102**, 770–776 (1998).
11. Fu, L. et al. Time-resolved spectroscopic behavior of Fe_2O_3 and $ZnFe_2O_4$ nanocrystals. *J. Chem. Phys.* **120**, 3406–3413 (2004).
12. Fan, H. M. et al. Shape-controlled synthesis of single-crystalline Fe_2O_3 hollow nanocrystals and their tunable optical properties. *J. Phys. Chem. C.* **113**, 9928–9935 (2009).
13. Joly, A. G. et al. Carrier dynamics in α-Fe_2O_3 (0001) thin films and single crystals probed by femtosecond transient absorption and reflectivity. *J. Appl. Phys.* **99**, 053521 (2006).
14. Wang, G. et al. Facile synthesis of highly photoactive α-Fe_2O_3-based films for water oxidation. *Nano Lett.* **11**, 3503–3509 (2011).
15. Ling, Y. et al. Sn-doped hematite nanostructures for photoelectrochemical water splitting. *Nano Lett.* **11**, 2119–2125 (2011).
16. Sorenson, S. et al. Ultrafast carrier dynamics in hematite films: the role of photoexcited electrons in the transient optical response. *J. Phys. Chem. C.* **118**, 23621–23626 (2014).
17. Pendlebury, S. R. et al. Ultrafast charge carrier recombination and trapping in hematite photoanodes under applied bias. *J. Am. Chem. Soc.* **136**, 9854–9857 (2014).
18. Pendlebury, S. R. et al. Dynamics of photogenerated holes in nanocrystalline alpha-Fe_2O_3 electrodes for water oxidation probed by transient absorption spectroscopy. *Chem. Commun.* **47**, 716–718 (2011).
19. Pendlebury, S. R. et al. Correlating long-lived photogenerated hole populations with photocurrent densities in hematite water oxidation photoanodes. *Energy Environ. Sci.* **5**, 6304–6312 (2012).
20. Barroso, M. et al. Dynamics of photogenerated holes in surface modified alpha-Fe_2O_3 photoanodes for solar water splitting. *Proc. Natl Acad. Sci. USA* **109**, 15640–15645 (2012).
21. Barroso, M. et al. Charge carrier trapping, recombination and transfer in hematite (α-Fe_2O_3) water splitting photoanodes. *Chem. Sci.* **4**, 2724–2734 (2013).
22. Huang, Z. et al. In situ probe of photocarrier dynamics in water-splitting hematite (α-Fe_2O_3) electrodes. *Energy Environ. Sci.* **5**, 8923 (2012).
23. Bosman, A. & Van Daal, H. Small-polaron versus band conduction in some transition-metal oxides. *Adv. Phys.* **19**, 1–117 (1970).
24. Morin, F. Electrical properties of α-Fe_2O_3 and α-Fe_2O_3 containing titanium. *Phys. Rev.* **83**, 1005 (1951).
25. Nakau, T. Electrical conductivity of α-Fe_2O_3. *J. Phys. Soc. Jpn.* **15**, 727–727 (1960).
26. Adelstein, N. et al. Density functional theory based calculation of small-polaron mobility in hematite. *Phys. Rev. B* **89**, 245115 (2014).
27. Katz, J. E. et al. Observation of transient iron(II) formation in dye-sensitized iron oxide nanoparticles by time-resolved x-ray spectroscopy. *J. Phys. Chem. Lett.* **1**, 1372–1376 (2010).
28. Katz, J. E. et al. Electron small polarons and their mobility in iron (oxyhydr) oxide nanoparticles. *Science* **337**, 1200–1203 (2012).
29. Hayes, D. et al. Electronic and nuclear contributions to time-resolved optical and X-ray absorption spectra of hematite and insights into photoelectrochemical performance. *Energy Environ. Sci.* **9**, 3754–3769 (2016).
30. Carneiro, L. M. et al. Excitation-wavelength-dependent small polaron trapping of photoexcited carriers in alpha-Fe_2O_3. *Nat. Mater.* **16**, 819–825 (2017).
31. Husek, J. et al. Surface electron dynamics in hematite (alpha-Fe_2O_3): correlation between ultrafast surface electron trapping and small polaron formation. *Chem. Sci.* **8**, 8170–8178 (2017).
32. Biswas, S. et al. Highly localized charge transfer excitons in metal oxide semiconductors. *Nano Lett.* **18**, 1228–1233 (2018).

33. Vura-Weis, J. et al. Femtosecond $M_{2,3}$-edge spectroscopy of transition-metal oxides: photoinduced oxidation state change in α-Fe_2O_3. *J. Phys. Chem. Lett.* **4**, 3667–3671 (2013).
34. Pastor, E. et al. In situ observation of picosecond polaron self-localisation in alpha-Fe_2O_3 photoelectrochemical cells. *Nat. Commun.* **10**, 3962 (2019).
35. Lee, J. & Han, S. Thermodynamics of native point defects in alpha-Fe_2O_3: an ab initio study. *Phys. Chem. Chem. Phys.* **15**, 18906–18914 (2013).
36. Zhou, Z. et al. Understanding hematite doping with group iv elements: a DFT + U study. *J. Phys. Chem. C.* **119**, 26303–26310 (2015).
37. Ansari, N. et al. Hole localization in Fe_2O_3 from density functional theory and wave-function-based methods. *Phys. Rev. Mater.* **1**, 035404 (2017).
38. Ahart, C. S., Blumberger, J. & Rosso, K. M. Polaronic structure of excess electrons and holes for a series of bulk iron oxides. *Phys. Chem. Chem. Phys.* **22**, 10699–10709 (2020).
39. Gardner, R. F. G., Sweett, F. & Tanner, D. W. The electrical properties of alpha ferric oxide—II.: ferric oxide of high purity. *J. Phys. Chem. Solids* **24**, 1183–1196 (1963).
40. Dare-Edwards, M. P. et al. Electrochemistry and photoelectrochemistry of iron(III) oxide. *J. Chem. Soc., Faraday Trans. 1* **79**, 2027–2041 (1983).
41. Braun, A. et al. Direct observation of two electron holes in a hematite photoanode during photoelectrochemical water splitting. *J. Phys. Chem. C.* **116**, 16870–16875 (2012).
42. Su, Z. et al. Ultrafast elemental and oxidation-state mapping of hematite by 4d electron microscopy. *J. Am. Chem. Soc.* **139**, 4916–4922 (2017).
43. Rosso, K. M., Smith, D. M. & Dupuis, M. An ab initio model of electron transport in hematite (α-Fe_2O_3) basal planes. *J. Chem. Phys.* **118**, 6455–6466 (2003).
44. Iordanova, N., Dupuis, M. & Rosso, K. M. Charge transport in metal oxides: a theoretical study of hematite α- Fe_2O_3. *J. Chem. Phys.* **122**, 144305 (2005).
45. Liao, P., Toroker, M. C. & Carter, E. A. Electron transport in pure and doped hematite. *Nano Lett.* **11**, 1775–1781 (2011).
46. Liao, P. & Carter, E. A. Hole transport in pure and doped hematite. *J. Appl. Phys.* **112**, 013701 (2012).
47. Smart, T. J. & Ping, Y. Effect of defects on the small polaron formation and transport properties of hematite from first-principles calculations. *J. Phys.: Condens. Matter* **29**, 394006 (2017).
48. Zhou, Z., Long, R. & Prezhdo, O. V. Why silicon doping accelerates electron polaron diffusion in hematite. *J. Am. Chem. Soc.* **141**, 20222–20233 (2019).
49. Zhang, L. et al. Dynamics of photoexcited small polarons in transition-metal oxides. *J. Phys. Chem. Lett.* **12**, 2191–2198 (2021).
50. Akimov, A. V. & Prezhdo, O. V. The pyxaid program for non-adiabatic molecular dynamics in condensed matter systems. *J. Chem. Theory Comput.* **9**, 4959–4972 (2013).
51. Akimov, A. V. & Prezhdo, O. V. Advanced capabilities of the pyxaid program: Integration schemes, decoherence effects, multiexcitonic states, and field-matter interaction. *J. Chem. Theory Comput.* **10**, 789–804 (2014).
52. Craig, C. F., Duncan, W. R. & Prezhdo, O. V. Trajectory surface hopping in the time-dependent Kohn-Sham approach for electron-nuclear dynamics. *Phys. Rev. Lett.* **95**, 163001 (2005).
53. Runge, E. & Gross, E. K. U. Density-functional theory for time-dependent systems. *Phys. Rev. Lett.* **52**, 997–1000 (1984).
54. Marques, M. A. L. & Gross, E. K. U. Time-dependent density functional theory. *Annu. Rev. Phys. Chem.* **55**, 427–455 (2004).
55. Kronawitter, C. et al. Titanium incorporation into hematite photoelectrodes: theoretical considerations and experimental observations. *Energy Environ. Sci.* **7**, 3100–3121 (2014).
56. Pham, T. D. & Deskins, N. A. Efficient method for modeling polarons using electronic structure methods. *J. Chem. Theory Comput.* **16**, 5264–5278 (2020).
57. Rettie, A. J. et al. Unravelling small-polaron transport in metal oxide photoelectrodes. *J. Phys. Chem. Lett.* **7**, 471–479 (2016).
58. Katz, J. E. et al. Electron small polarons and their mobility in iron (oxyhydr)oxide nanoparticles. *Science* **337**, 1200–1203 (2012).
59. Zhou, Z. et al. Control of charge carriers trapping and relaxation in hematite by oxygen vacancy charge: Ab initio non-adiabatic molecular dynamics. *J. Am. Chem. Soc.* **139**, 6707–6717 (2017).
60. Nelson, T. R. & Prezhdo, O. V. Extremely long nonradiative relaxation of photoexcited graphane is greatly accelerated by oxidation: time-domain ab initio study. *J. Am. Chem. Soc.* **135**, 3702–3710 (2013).
61. Liu, J. et al. Ligands slow down pure-dephasing in semiconductor quantum dots. *ACS Nano* **9**, 9106–9116 (2015).
62. Akimov, A. V. & Prezhdo, O. V. Persistent electronic coherence despite rapid loss of electron–nuclear correlation. *J. Phys. Chem. Lett.* **4**, 3857–3864 (2013).
63. Mukamel, S. *Principles of Nonlinear Optical Spectroscopy* (Oxford University Press, 1995).
64. Chamritski, I. & Burns, G. Infrared- and Raman-active phonons of magnetite, maghemite, and hematite: a computer simulation and spectroscopic study. *J. Phys. Chem. B* **109**, 4965–4968 (2005).
65. Zhang, M. et al. Improved photoelectrochemical responses of Si and Ti codoped α-Fe_2O_3 photoanode films. *Appl. Phys. Lett.* **97**, 042105 (2010).
66. Fan, Y. et al. Intrinsic polaronic photocarrier dynamics in hematite. *Phys. Rev. B* **103**, 085206 (2021).
67. Liao, H. et al. Micro-heterogeneous annihilation dynamics of self-trapped excitons in hematite single crystals. *J. Phys. Chem. Lett.* **11**, 7867–7873 (2020).
68. Fan, Y. et al. Recombination of polaronic electron–hole pairs in hematite determined by nuclear quantum tunneling. *J. Phys. Chem. Lett.* **12**, 4166–4171 (2021).
69. Fischer, S. A. et al. Regarding the validity of the time-dependent Kohn-Sham approach for electron-nuclear dynamics via trajectory surface hopping. *J. Chem. Phys.* **134**, 024102 (2011).
70. Jaeger, H. M., Fischer, S. & Prezhdo, O. V. Decoherence-induced surface hopping. *J. Chem. Phys.* **137**, 22A545 (2012).
71. Long, R. et al. Donor–acceptor interaction determines the mechanism of photoinduced electron injection from graphene quantum dots into TiO_2: Π-stacking supersedes covalent bonding. *J. Am. Chem. Soc.* **139**, 2619–2629 (2017).
72. Long, R. & Prezhdo, O. V. Instantaneous generation of charge-separated state on TiO_2 surface sensitized with plasmonic nanoparticles. *J. Am. Chem. Soc.* **136**, 4343–4354 (2014).
73. Kresse, G. & Furthmüller, J. Efficient iterative schemes for ab initio total-energy calculations using a plane-wave basis set. *Phys. Rev. B* **54**, 11169–11186 (1996).
74. Tully, J. C. Molecular dynamics with electronic transitions. *J. Chem. Phys.* **93**, 1061–1071 (1990).

ACKNOWLEDGEMENTS

This work was supported by the National Science Foundation of China, grant Nos. 51861135101, 21973006, 21688102, and 21590801. R.L. acknowledges financial support by the Recruitment Program of Global Youth Experts of China and the Beijing Normal University Startup. Z.Z. acknowledges financial support by the Natural Science Basic Research Program of Shaanxi Province (2019JQ-440).

AUTHOR CONTRIBUTIONS

R.L., Z.H.Z., and W.H.F. conceptualized the work. The simulations were performed by C.C. and Y.H.Z. The paper was written by R.L., Z.H.Z., and C.C. with input from W.H.F. All authors contributed to the discussions and analyses of the data and approved the final version.

COMPETING INTERESTS

The authors declare no competing interests.

ADDITIONAL INFORMATION

Supplementary information The online version contains supplementary material available at https://doi.org/10.1038/s41524-022-00814-7.

Correspondence and requests for materials should be addressed to Zhaohui Zhou or Run Long.

Reprints and permission information is available at http://www.nature.com/reprints

Publisher's note Springer Nature remains neutral with regard to jurisdictional claims in published maps and institutional affiliations.